Device

Article

Fluorescent hydrogel platform for 3D information storage and encryption anti-counterfeiting

Graphical abstract

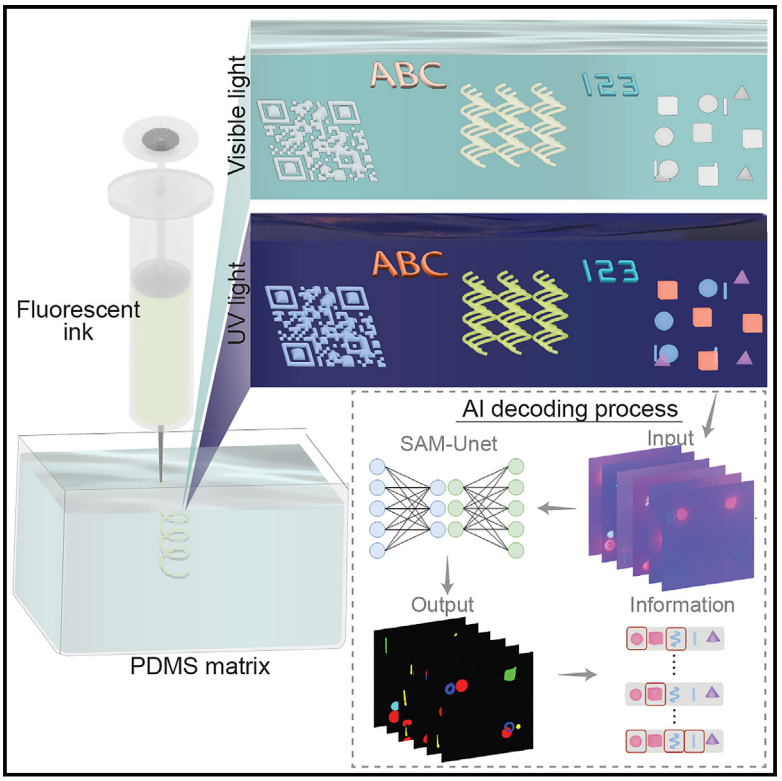

Highlights

- Precision printing of 2D patterns and 3D structures within a polymer matrix
- Robust 3D PUFs resistant to physical and chemical threats
- AI decrypts 3D PUFs for secure data and advanced interaction
- Integrates fluorescent materials with AI and additive manufacturing

Authors

Shitong Zhou (周诗桐), Fengyu Lin (林逢雨), Qingwen Guan (管晴雯), Lan Ding (丁兰), Eduardo Saiz, Ming Li (李明)

Correspondence

e.saiz@imperial.ac.uk (E.S.), m.li19@alumni.imperial.ac.uk (M.L.)

In brief

Despite the widespread use of fluorescent materials for encryption and anti-counterfeiting, their application has largely been limited to 2D surfaces prone to damage. Our study addresses this with a one-step method using specialized fluorescent hydrogel inks and PDMS matrices, developed through a deep understanding of rheology. This facilitates embedded printing of complex 2D and 3D patterns, enabling on-demand encryption and decryption via physical unclonable functions and an AI recognition model, enhancing material functionality and security.

3 **Develop**
Prototype with demonstrated applications in relevant environment

Zhou et al., 2025, Device *3*, 100722
June 20, 2025 © 2025 The Author(s). Published by Elsevier Inc.
https://doi.org/10.1016/j.device.2025.100722

CellPress

Device

CellPress
OPEN ACCESS

Article

Fluorescent hydrogel platform for 3D information storage and encryption anti-counterfeiting

Shitong Zhou (周诗桐),[1] Fengyu Lin (林逢雨),[1] Qingwen Guan (管晴雯),[2] Lan Ding (丁兰),[3] Eduardo Saiz,[1,*] and Ming Li (李明)[1,4,*]

[1]Centre for Advanced Structural Ceramics, Department of Materials, Imperial College London, London SW7 2AZ, UK
[2]School of Chemistry, University of Glasgow, Glasgow G12 8QQ, UK
[3]College of Pharmacy, Dali University, Dali City, Yunnan 671000, China
[4]Lead contact
*Correspondence: e.saiz@imperial.ac.uk (E.S.), m.li19@alumni.imperial.ac.uk (M.L.)
https://doi.org/10.1016/j.device.2025.100722

THE BIGGER PICTURE This research introduces a groundbreaking 3D fluorescent hydrogel platform, meticulously designed to revolutionize anti-counterfeiting and encryption practices. Our method significantly advances beyond the traditional 2D approaches, which are susceptible to environmental and physical disruptions. By harnessing embedded printing techniques, we engineer robust 3D structures that remain undetectable under normal lighting conditions but reveal their intricate details under ultraviolet (UV) light. This feature of dual visibility is crucial for enhancing security. In addition to improved durability, our platform incorporates the novel use of physical unclonable functions (PUFs), which are virtually impossible to replicate. This encoding strategy significantly bolsters security by embedding unique, tamper-evident patterns directly into the structure of the material. An AI-driven recognition model complements this approach by providing precise and efficient decryption of these complex patterns, setting a new standard in secure material technology. This technological leap not only elevates the security measures to unprecedented levels but also pioneers the use of intelligent, functional materials within the security sector. The integration of advanced materials science with AI opens new avenues for the development of smart security solutions that are both effective and adaptable. By setting a new benchmark for anti-counterfeiting technologies, this research not only protects against fraudulent activities but also facilitates the evolution of security protocols in various industries, from pharmaceuticals to luxury goods. This work promises to transform the landscape of material-based security, making it an essential cornerstone for future innovations in the field.

SUMMARY

Information security and anti-counterfeiting are crucial across diverse sectors. We propose a method that integrates fluorescent-responsive materials with advances in additive manufacturing and artificial intelligence (AI) to enhance encryption technologies. Our approach employs 3D fluorescent hydrogel structures embedded within a protective polymer matrix using printing techniques, enhancing stability and damage resistance. This allows for constructing complex hierarchical patterns in both two and three dimensions—pixels and voxels—beyond traditional methods dependent on preformed templates. By incorporating materials that adjust visibility under different lighting, combined with additive fabrication, our method supports dual encryption through visible/UV light switching and uses a physical unclonable function (PUF) for secure 3D encrypted data. A machine learning AI model efficiently decrypts these PUF patterns, promoting advanced material-machine interaction. This work offers new avenues in encryption processing by merging nanotechnology with structural manipulations up to the macrolevel, setting the stage for developing practical 3D fluorescent anti-counterfeiting hydrogels.

INTRODUCTION

Encryption is a critical technology in military and civilian applications that rely on the secure transfer and storage of information.[1–3] Recent advances are the development of diverse encryption and anti-counterfeiting technologies using pattern recognition,[4–7] such as holograms, watermarks, security codes, and fluorescent patterns, with the latter gaining attention for their

This is an open access article under the CC BY-NC license (http://creativecommons.org/licenses/by-nc/4.0/).

vivid color changes, possibility of tuning the spectral response, and rapid response to stimuli.[8–10] To date, research on fluorescent-responsive encryption materials has predominantly focused on the design and synthesis of innovative light-emitting sources, including organic dyes,[11] fluorescent compounds,[12] lanthanide complexes,[13] aggregation-induced emission molecules,[14] and fluorescent quantum dots.[10,15,16] A significant effort has also been made in the development of multi-responsive color-rendering techniques to enhance security, combining structural and fluorescent colors or employing "dual/multi-channel" stimulus-response modes as a way to obtain switchable two-dimensional (2D) codes.[17–19]

Despite the significant advances and great potential, several critical challenges remain in the development of encryption based on fluorescent materials. Most methods for their implementation, such as inkjet or mold printing, are restricted to 2D surfaces and vulnerable to degradation (e.g., wear, impact, detachment), which can compromise the encoded information.[20,21] More secure approaches often require complex operations, lengthy preparation times, and costly equipment, limiting their commercial scalability. For instance, manually assembling hydrogel blocks into pixelated arrays or quick-response (QR) codes for dynamic encryption under dual/multiple stimuli is time-consuming and space intensive, making it impractical for large-scale applications.[22] Methods like direct laser writing or lithography can reduce the size of the target pixels to 100 nm and enhance stability but involve laborious steps such as grid writing, fluorescent labeling, cleaning of residuals, and pattern generation.[23,24] Additionally, the reliability of the encrypted information depends significantly on the concentration of the fluorescent source; too low a concentration results in prolonged decryption times, whereas too high a concentration may distort the data.[24–27]

Given these limitations, there is an urgent need to develop technologies for the fast and easy fabrication of reliable and resilient multidimensional fluorescent encryption materials. Embedded three-dimensional (3D) printing, a variant of direct ink writing (also known as robocasting), offers the potential to customize 2D and 3D patterns inside a matrix without the need for additional supports.[28] This technology has been applied in various contexts, such as the fabrication of polymer-based composites, drug-delivery capsules, or complex structural parts.[29–31] Embedded 3D printing is particularly well suited for designing reliable and stable 2D or 3D fluorescent patterns in anti-counterfeiting applications. The simplicity in the preparation of fluorescent sources (e.g., quantum dots, luminous powder, luminous paint) with high color purity that can be dispersed homogeneously in polymer inks enables the tuning of fluorescent colors across the visible spectrum.[32] Moreover, traditional decipherment methods, which typically require manual identification and are inefficient for large volumes of encrypted information, could be enhanced by developing an intelligent recognition model. This model would leverage novel artificial intelligence (AI) techniques in image recognition to improve the efficiency of reading encrypted patterns and decoding information.[33–35]

In this work, we have successfully printed 2D and 3D hydrogel patterns/structures responsive to UV light inside a polydimethylsiloxane (PDMS) matrix using a temperature-sensitive Pluronic ink. The ink consists of a uniform dispersion of different fluorescent sources and is printed into the PDMS matrix and subsequently cured. To ensure that the printed structures retain their shape, the rheology of the PDMS is manipulated using fumed silica to form a transparent matrix. This method safeguards the fluorescent-responsive structure within the matrix from physical and chemical damage. It allows for the incorporation of diverse 2D pixel and 3D voxel structures, with dimensions ranging from tens to hundreds of microns, all exhibiting fluorescent-responsive properties. Our approach not only enhances the security and complexity of the encrypted information but also facilitates on-demand decoding using encryption based on physical unclonable functions (PUFs), thus boosting the reliability of the encrypted data.[5,36] To expedite the recognition and authentication process, we have also developed an AI recognition model, streamlining the process from fluorescent image capture to encrypted information deciphering. This advancement fosters the development of smart materials with integrated material-machine interaction functionalities, providing fresh insights into the construction of multidimensional fluorescent hydrogel structures for anti-counterfeiting.

RESULTS AND DISCUSSION

The fabrication of fluorescent-responsive 3D anti-counterfeiting hydrogels hinges on the development of embedded fluorescent patterns, through the careful selection of the printing ink and the support matrix. In our research, we opted for a Pluronic 127 hydrogel as the base for the ink due to its compatibility with various fluorescent sources and its printability. The choice of Pluronic-based inks is primarily driven by two factors: first, they exhibit a shear-thinning behavior (Figure S1), which enables continuous and stable extrusion to build the desired structures[37]; second, both water- and oil-soluble fluorescent sources can be uniformly dispersed in Pluronic hydrogels (Figure S2), as required, to prepare fluorescent-responsive inks for reliable printing. This is due to its amphiphilic nature and the formation of a stable micelle network above its critical concentration (Figure S3).[38]

The selection of the support matrix is crucial for successful embedded printing. For this study, a PDMS mixture composed of Sylgard 184 and SE 1700 was used (Figure 1A). The former is a flowable silicone elastomer, whereas the latter, containing ~20 wt % fumed silica as a rheological modifier, is non-flowing.[28] This choice is justified by several key properties of the PDMS mixture: (1) it is immiscible with Pluronic-based inks, preventing diffusion of the ink into the matrix during printing, thus preserving the integrity/fidelity of the printed structures (Figure S4); (2) its density is similar to that of Pluronic gels, which helps to support the printed structures without the displacement or distortion caused by gravitational or buoyant forces; (3) it enables ink extrusion inside by maintaining good fluidity and low viscosity near the nozzle during printing; (4) it bonds well with the Pluronic-based inks, facilitating the elimination of gaps during printing; and (5) its rheological properties and transparency can be adjusted by varying the ratio of Sylgard 184 to SE 1700, enhancing the control over the printing process and the masking of embedded information. In addition, its excellent mechanical properties, such as high tear resistance and solvent

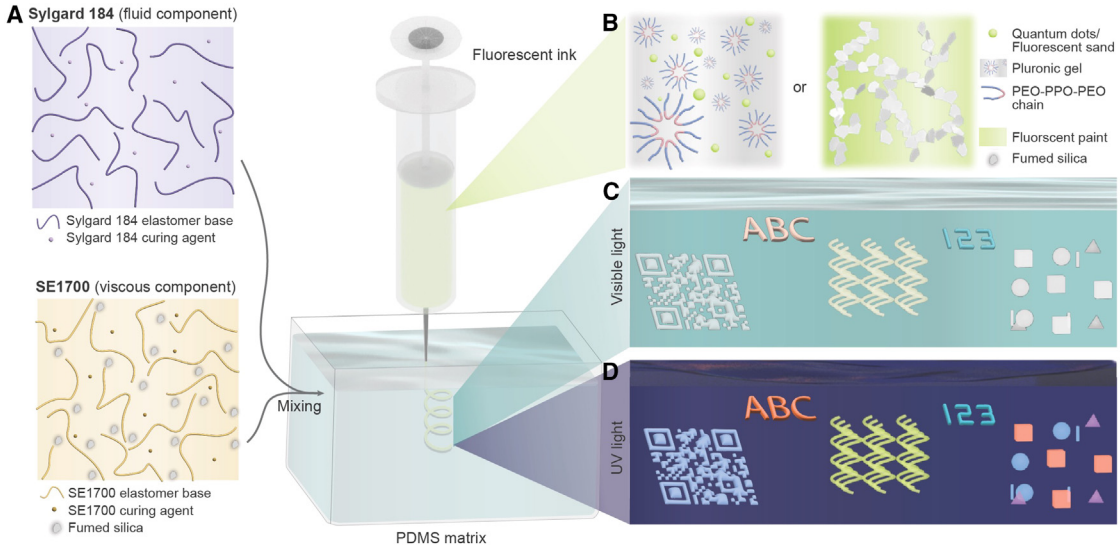

Figure 1. Embedded fluorescent patterns in a PDMS matrix

(A) Schematic of the printing process highlighting the components of the PDMS matrix, including Sylgard 184 and SE 1700.

(B) Depiction of two types of fluorescent inks: one containing quantum dots or fluorescent sand in Pluronic hydrogel, and the other containing fluorescent paint and fumed silica.

(C) Printed 2D patterns under visible light.

(D) Printed 3D patterns under UV light, showcasing the distinct fluorescence emitted by each ink type.

resistance, make PDMS exceptionally suitable for creating durable and stable structures. In this study, PDMS serves a dual role: it acts as both an encapsulant and a supporting matrix.

As illustrated in Figure 1, by strategically positioning the printing nozzle, a Pluronic hydrogel ink (Figure 1B) laden with fluorescent sources can be omnidirectionally printed within the PDMS matrix, enabling the creation of diverse 2D patterns and 3D structures. The viscosity and yield stress of the ink and matrix as well as their densities (1.01 g/cm^3 for the ink and 0.97 g/cm^3 for the matrix) are carefully matched such that the printed patterns and structures remain stable in their designated positions, effectively preventing the loss of information caused by the displacement or distortion of the printed elements. To demonstrate this capability, we have successfully printed fluorescent inks within the PDMS matrix to prepare embedded fluorescent-responsive anti-counterfeiting hydrogel structures with various 2D patterns such as letters, numbers, and QR codes, as well as 3D structures like helical spirals and spheres (Figures 1C and 1D). Detailed printing parameters are introduced in the following sections.

Rheological and printing properties of substrate and ink

The fidelity and accuracy of the embedded structures are critically influenced by the rheology of the matrix and ink, as well as the printing parameters. Initially, we explored the rheology of the PDMS matrix. We observed that structures printed in a matrix composed solely of Sylgard 184 were displaced by the nozzle during printing. This is due to the nature of this matrix, which behaves as a Newtonian fluid with low viscosity compromising printing fidelity (Figure S5; Video S1). An ideal matrix for embedded printing should be shear thinning with yield stress low enough to facilitate extrusion inside and high enough to hold the embedded structure. Furthermore, matching of the viscosities of matrix and ink is needed to retain filaments with close to circular cross-section.[28,39–41] To address these issues, we enhanced the viscosity of the support matrix by incorporating SE 1700 in Sylgard 184. SE 1700 is a PDMS variant known for its higher viscosity and contains ~20 wt % fumed silica.[42] As depicted in Figure 2A, the modified matrix exhibits increased viscosity and more pronounced shear thinning, with viscosity decreasing with increasing shear rate ($\dot{\gamma}$). At low SE 1700 contents (<45 wt %), the embedded printed patterns were dragged and deformed (Figure S6A). Conversely, at high SE 1700 contents (≥60 wt %), the matrix became too viscous with a high yield stress, resulting in the formation of persistent air bubbles and an uneven surface (Figure S6B). Matrices with SE 1700 contents ranging between 45 and 50 wt % enabled stable embedded printing while retaining smooth surfaces. To further elucidate the impact of SE 1700 concentration, we analyzed the flow behavior of matrices with varying compositions, which was subsequently fitted using the Herschel-Bulkley equation,[43]

$$\tau = \tau_y + K\dot{\gamma}^n,$$

where τ is the shear stress, τ_y is the yield stress, n is the shear-thinning coefficient, and K is the viscosity parameter. In addition, the experimental flow point, τ_f, which is identified as the crossover point of storage and loss moduli in oscillatory tests (Figure 2B), was also used as a measure of the stress required to change the matrix behavior from solid to liquid-like. According to Table S1 and Figure 2B, the matrix yield stress, τ_y, as calculated from the Herschel-Bulkley formula, closely matched the

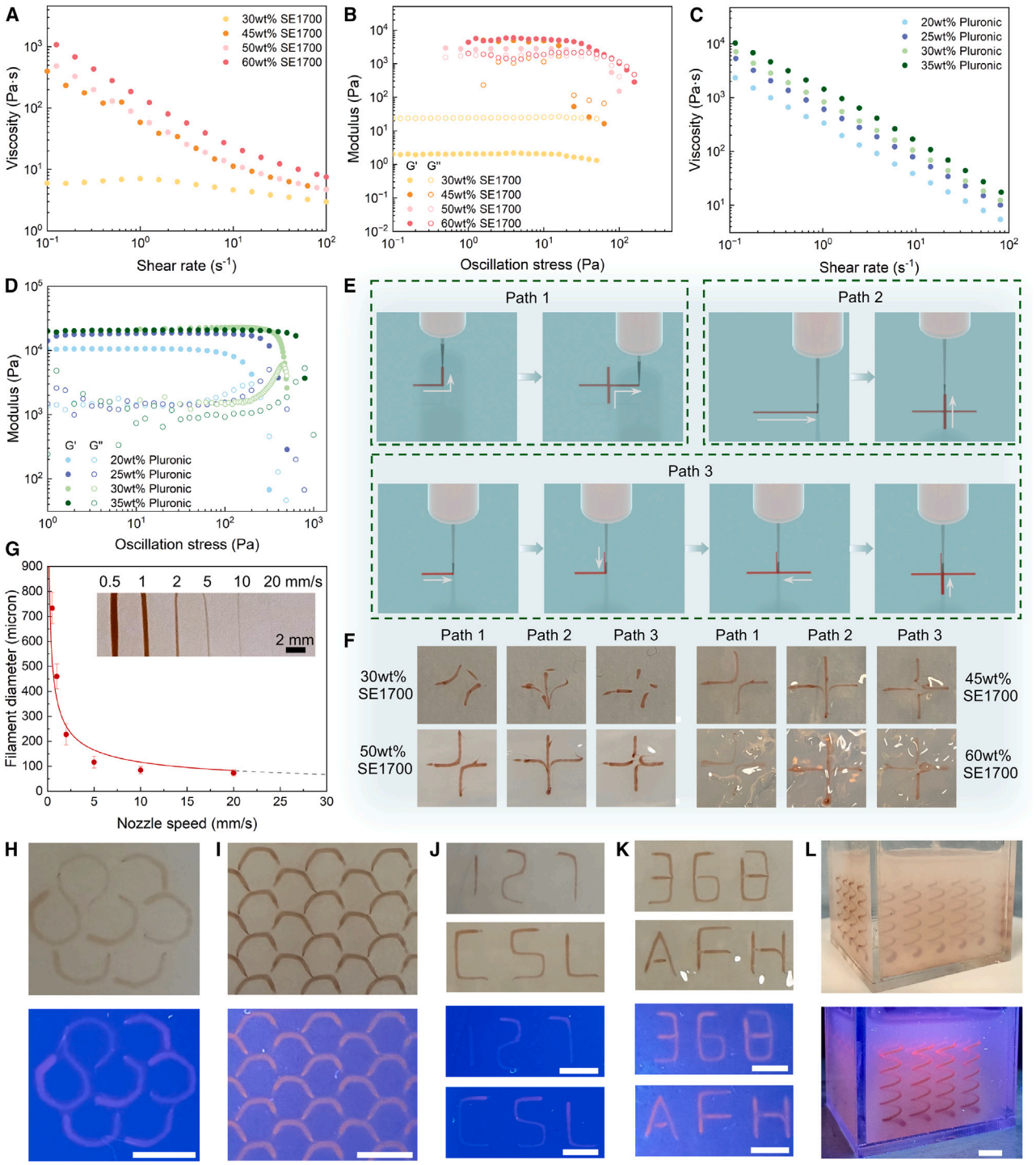

Figure 2. Rheological properties and printing parameters of embedded fluorescent patterns

(A) Flow curve illustrating the viscosity of the polymer matrix across varying SE 1700 concentrations.

(B) Oscillatory rheology measurements of the viscoelastic properties of the polymer matrix with different SE 1700 contents.

(C) Flow curve of the hydrogel ink showing changes in viscosity with different Pluronic concentrations.

(D) Oscillatory rheology measurements of the hydrogel ink, showing its viscoelastic behavior at various Pluronic levels.

(E) Schematics of different printing paths used during the study.

(F) Images of structures printed in various matrices along three different paths, demonstrating the adaptability of the printing process.

(legend continued on next page)

τ_fs, confirming the reliability of the τ_y, K, and n values obtained from the fittings. Increasing the SE 1700 content increases the K and reduces the n. This increase in viscosity is due to a higher concentration of fumed silica that hinders the relative motion of polymer chains and effectively prevents nozzle drag of the printed structure (Figure S7).

Given that micellization is influenced by temperature and Pluronic concentration,[44,45] selecting inks with suitable Pluronic concentrations is crucial for achieving uniform fluorescent source distribution and successful embedded printing. At 25°C, inks with Pluronic concentrations between 25 and 35 wt % exhibited the shear-thinning behavior required for printing (Figure 2C). Below 25 wt %, the ink remained too fluid at room temperature and without the yield stress required to resist distortion and maintain the shape of the printed parts (Figures S8 and S9). In contrast, inks with more than 35 wt % Pluronic formed stable micelle networks even at 10°C, hampering the dispersion of quantum dots and leading to unstable, hard-to-extrude inks (Figures S8 and S9). This is because the inks' viscosity, equilibrium storage modulus, and flow point increase as the Pluronic concentration in the ink increases (Figures 2C and 2D). As a result, we selected a 30 wt % Pluronic gel as a carrier for quantum dots that enables homogeneous dispersion and stable printing across varying temperatures. Interestingly, when different concentrations of fluorescent quantum dots (1–40 wt %, equivalent to 1–40 vol % for blue and green carbon dots and 1–47 vol % for red carbon dots) were added to the Pluronic gel, the resulting inks still exhibited similar shear-thinning behavior and consistent rheological properties at various shear rates (Figure S10). This suggests that when the quantum dots are introduced in the Pluronic gel network, they can endow the ink with fluorescent properties without affecting the rheology.

The quality of the printed patterns also depends on the choice of printing path.[42] We investigated the effects of three different paths (Figure 2E). Path 1, which involved printing a cross in two parts at right angles, and paths 2 and 3, which divided the cross into two and four parts, respectively, were printed in a clockwise sequence. Each path differed in how the nozzle moved between print segments, impacting the continuity and alignment at the intersections. Specifically, in each path, after printing a segment, the nozzle tip ascends in the z-direction, shifts horizontally to the designated position, and then descends to the initial depth before commencing the next segment of the pattern. We utilized an ink formulation consisting of 30 wt % Pluronic and 12.5 wt % red fluorescent quantum dots (R-CDs), extruded through a nozzle tip with a radius, R, of 410 μm at a speed of 2 mm/s (with a piston extrusion rate of 0.0037 mm/s). As illustrated in Figure 2F, paths 1 and 3 led to discontinuities and distortions at the central intersection of the cross. In contrast, path 2 yielded crosses with properly intersecting centers, although slight misalignments were observed, which could be rectified by utilizing printing nozzles with smaller inner diameters (Figure S11). This demonstrates that for patterns or structures involving multiple strokes, selecting the appropriate print path is crucial, whereas this factor may be less significant for single-stroke designs. For the former, the selection of a proper print path involves, first, dividing the structure in as few parts as possible and, second, avoiding retraction and insertion; this can be automated using an algorithm.[46] Furthermore, we can regulate precisely the diameter of the printed filaments by adjusting the moving speed of the nozzle.[29] By progressively altering the nozzle translation speed, V, from 0.5 to 20 mm/s while maintaining a constant piston extrusion rate V_e, we established that the diameter of the filaments d in cured matrices is inversely proportional to the square root of the velocity, $d \propto \sqrt{\frac{4 \times R^2 \times V_e}{V}}$ (Figure 2G). This relationship enables us to accurately adjust the diameter of the line extruded through a 410-μm nozzle from 70 to 700 μm, simply by modifying V. This feature is particularly advantageous for rapid printing of complex patterns such as barcodes (Figure 2G, inset).

To further assess the impact of matrix composition and print path on pattern fidelity, we printed basic intersecting geometries (i.e., crosses) in matrices with varying SE 1700 contents (from 30 to 60 wt %) using the described print paths (Figure 2F). The pattern printed with path 2 in matrices containing over 45 wt % SE 1700 most closely matched its intended design. At lower SE 1700 contents, patterns were dragged by the nozzle, while higher contents (>60 wt %) led to air bubbles and uneven surfaces. With the optimal matrix containing 50 wt % SE 1700, we successfully fabricated a variety of one-stroke and multi-stroke 2D planar patterns and 3D spatial structures in PDMS, such as flower petals (Figure 2H), fish scales (Figure 2I), numbers and letters (Figures 2J and 2K), and a 3D spiral structure (Figure 2L).

Fluorescent behavior of ink

The fluorescent-responsive behavior of hydrogel composites is derived from the photoluminescent properties of the fluorescent materials incorporated into the ink. Fluorescent quantum dot inks that can be observed under visible light cannot conceal encrypted information (Figures 2H–2L). To address this problem, we synthesized R-CDs, green (G-CDs), and blue (B-CDs) fluorescent carbon quantum dots using a hydrothermal method.[10,15] These dots were selected to explore their information-masking properties under visible light. They are spherical, with a uniform and narrow size distribution ranging from 1 to 5 nm in diameter, indicating a highly size-selective synthesis process (Figure S12). Under visible light, the R-/G-/B-CDs appeared red, orange, and colorless, respectively. However, under 365 nm UV light, these solutions exhibited distinct red, green, and bright blue fluorescence (Figure S13). Thus, only the ink containing blue carbon quantum dots effectively masks information under visible light while revealing hidden information through blue fluorescence under UV light. To evaluate the impact of the B-CD content on the photoluminescence of the ink, we varied the mass fraction of B-CDs in Pluronic gels and analyzed their photoluminescence

(G) Graph showing the variation in filament diameter relative to nozzle speed, with a constant extrusion rate; error bars represent the standard deviation from 15 measurements across 3 different prints.
(H–L) Examples of embedded 2D and 3D patterns containing 30 wt % Pluronic and 12.5 wt % red carbon dots within a PDMS matrix comprising 50 wt % SE 1700. Scale bar: 0.5 mm.

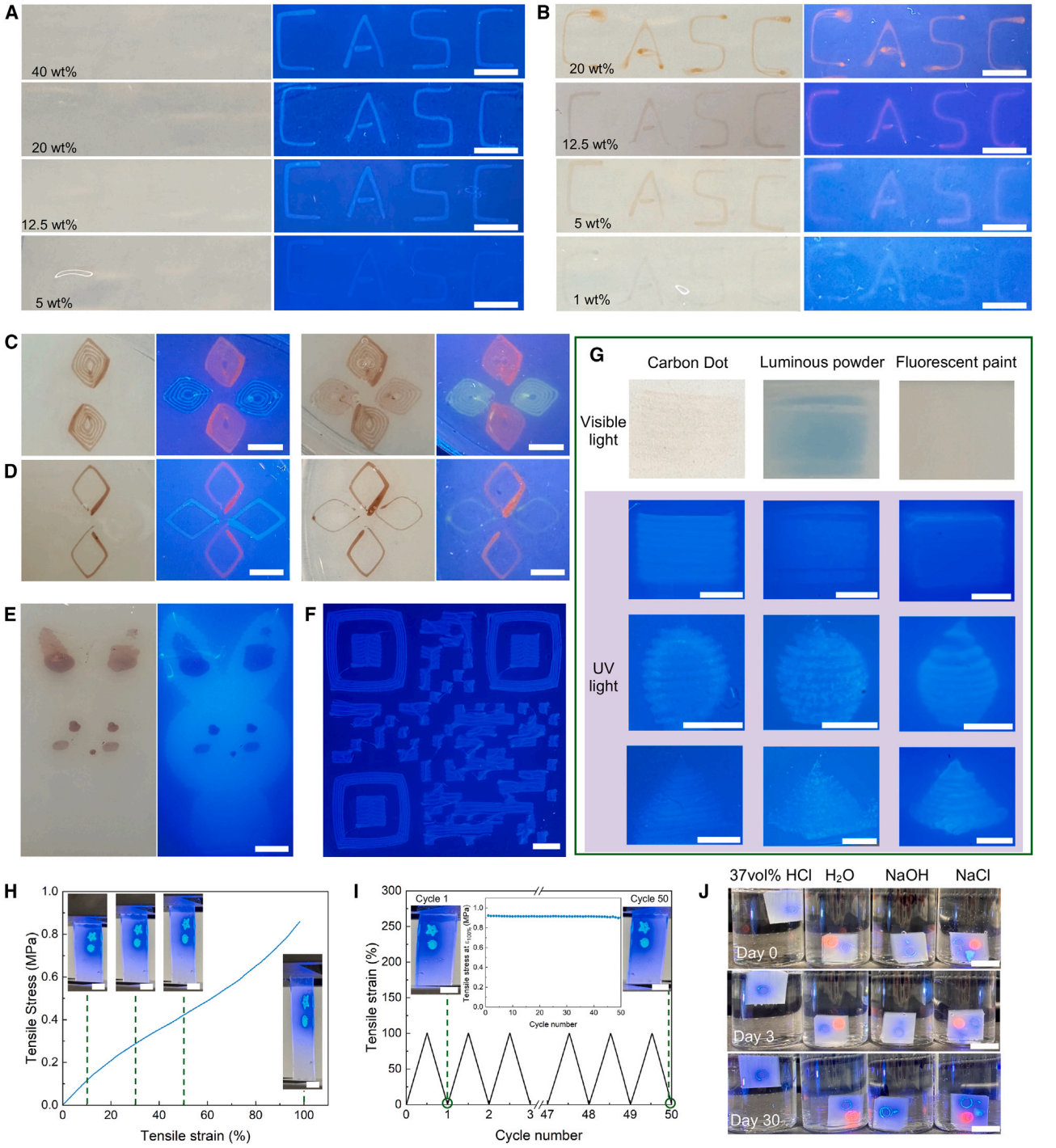

Figure 3. Fluorescence and mechanical properties of embedded printed structures

(A) Inks with varying concentrations of blue carbon dots (B-CDs) in Pluronic gel within PDMS, shown under visible and UV light. Concentrations from bottom to top are 5, 12.5, 20, and 40 wt %. Scale bar: 0.5 mm.

(B) Inks with varying concentrations of red carbon dots (R-CDs) in Pluronic gel within PDMS, displayed under visible and UV light. Concentrations from bottom to top are 1, 5, 12.5, and 20 wt %. Scale bar: 0.5 mm.

(C–G) Examples of printed 2D and 3D structures featuring various designs and colors. (C) Multicolor flower petals, demonstrating the use of different fluorescent inks. Scale bar: 0.5 mm. (D) A rhombohedral pattern, showcasing precision in geometric printing. Scale bar: 0.5 mm. (E) Rabbit shapes, illustrating detailed and precise figure replication. Scale bar: 0.5 mm. (F) A QR code that links to baidu.com, emphasizing practical applications of encrypted information. Scale bar: 0.5 mm. (G) The 3D structures created using different fluorescent materials: carbon dot, luminous powder, and fluorescent paint, shown from left to right. Scale bar: 0.2 mm.

(legend continued on next page)

spectra. Increasing the B-CD content from 1 to 40 wt % did not alter the absorption band shape of the ink, which consistently exhibited blue fluorescence (Figure S14). The fluorescence of inks with less than 5 wt % B-CD was barely visible to the naked eye; however, fluorescence intensity increased significantly between 5 and 20 wt %, stabilizing at concentrations above 20 wt %. As demonstrated in Figure S14B, while changes in B-CD content influenced the fluorescence intensity at the emission peak, they did not affect the spectral band shape. This confirms that the fluorescent intensity of printed structures within the matrix can be controlled by adjusting the concentration of fluorescent quantum dots in the ink.

We utilized Pluronic inks with varying concentrations of R-CDs (1–20 wt %) and B-CDs (5–40 wt %) to print patterns within a support matrix containing 50 wt % SE 1700. The resulting embedded fluorescent encrypted samples are depicted in Figures 3A and 3B. Under visible light, patterns printed with blue fluorescent ink remain invisible, whereas those printed with red fluorescent ink are visible to the naked eye. Under UV light, inks with less than 5 wt % B-CDs fail to reveal the printed patterns post-curing, and patterns printed with more than 20 wt % B-CDs do not show a significant change in fluorescent intensity discernible to the human eye or camera, consistent with the fluorescence spectra (Figure S14). Consequently, 20 wt % B-CD was determined to be the optimal concentration for subsequent printing. Similarly, patterns printed with 1 wt % R-CDs exhibit the weakest fluorescent intensity under UV light, making them difficult to detect; patterns with R-CD concentrations above 12.5 wt % do not exhibit significant changes in fluorescent intensity (Figure 3B). It is important to note that higher concentrations of R-CDs can lead to uneven distribution and fluorescence brightness in the pattern. Therefore, an optimized concentration of 12.5 wt % R-CDs was selected.

By strategically combining blue fluorescent ink, which masks information under visible light, with red and green inks that do not, we can embed encrypted information within the matrix through 3D printing. As demonstrated in Figure S15, the visible information reads "OLD," "ICE," and "EAT," while under UV light, the true encrypted messages "COLD," "RICE," and "MEAT" are revealed. This innovative encryption approach can be further applied to create a variety of customized geometries, such as multicolored flower petals (Figure 3C), rhombus combination patterns (Figure 3D), and rabbits (Figure 3E). Additionally, by mixing three different types of quantum dots, we achieved a full-spectrum modulation of fluorescent inks to diversify print colors (Figure S16), exemplified by the yellow petals in Figure 3C and variably colored rabbits in Figure S17.

Beyond planar patterns, our method allows for direct printing of QR codes within the PDMS matrix, invisible under visible light but revealing a scannable QR code under UV light (Figure 3F). Scanning this QR code with a suitable application directs the mobile phone to a corresponding web page (Video S2). While our experiments underscore the advantages of embedded printing in creating fluorescent encryption materials, current applications have been limited to 2D patterns. The significant innovation of embedded 3D printing, as opposed to earlier methods, lies in its capacity to create complex 3D structures like pyramids, cubes, and spheres directly within the support matrix (Figure 3G). To expand the versatility of this technique, we also used commercial luminous powder and fluorescent paint as alternative fluorescent sources for creating 3D structures. It should be noted that while the luminous powder can be directly mixed into Pluronic gel, the fluorescent paint forms flocs upon contact with water, losing its printability (Figure S18), unless it is mixed with a rheological modifier such as fumed silica (Figure 3G). The rheological properties of this modified ink are detailed in Table S1.

The cured PDMS matrix offers excellent protection for the embedded fluorescent information, effectively preventing loss or damage due to physical or chemical external factors that often compromise previous fluorescent encryption materials. As demonstrated in Figure 3H, the embedded structures deformed along with the PDMS matrix under a tensile stress of up to 0.9 MPa. Upon removal of the external force, both the PDMS matrix and the embedded structures successfully returned to their original shapes (Video S3). Remarkably, the fluorescent structures remained intact even after 50 loading cycles (100% strain), underscoring their small elastic hysteresis and exceptional tensile resilience within the composite (Figures 3I and S19). They also exhibit notable compressive resistance (Figure S20). For example, even after the PDMS composite, which contained an embedded fluorescent QR code, was subjected to stretching and compression, the QR code remained decipherable under UV light using a mobile phone application (Video S4). Furthermore, the protective properties of the exterior PDMS matrix effectively shielded the fluorescent patterns and structures within the composites from damage when subjected to harsh conditions. These conditions included high humidity; exposure to strong acids, strong bases, and high salt solutions over an extended period of 30 days; prolonged UV exposure for several hours; and drastic temperature fluctuations ranging from −12°C to 160°C (the upper limit of the operating temperature to ensure that the color does not fade is ∼120°C). Notably, despite these challenging environments, the fluorescent patterns and structures maintained their ability to emit light under UV exposure, as demonstrated in Figures 3J, S21, and S22.

3D encryption design based on PUFs

The flexibility of embedded 2D patterns in pixels and 3D structures in voxels, combined with the versatility of fluorescent inks in terms of colors, spectral responses, and materials, lays the groundwork for constructing a high-security encryption system based on PUFs.[5] A PUF is a function that defines the relationship

The unexpected fluorescent spreading in (A)–(G) could be related to cross-contamination of the matrix during handling or by small amounts of ink attached to the nozzle surface.

(H) Tensile stress-strain curve for PDMS embedded with fluorescent structures, demonstrating the mechanical properties of the material. Scale bar: 5 mm.

(I) Cycling tensile test showing the resilience of the material over 50 tensile tests to 100% strain ($\varepsilon_{100\%}$). Scale bar: 5 mm.

(J) Durability of 3D fluorescent structures in PDMS when immersed in various harsh environments: 37 vol % HCl (pH 1), deionized water, NaOH (pH 14), and saline water, all under UV light for 30 days. Scale bar: 10 mm.

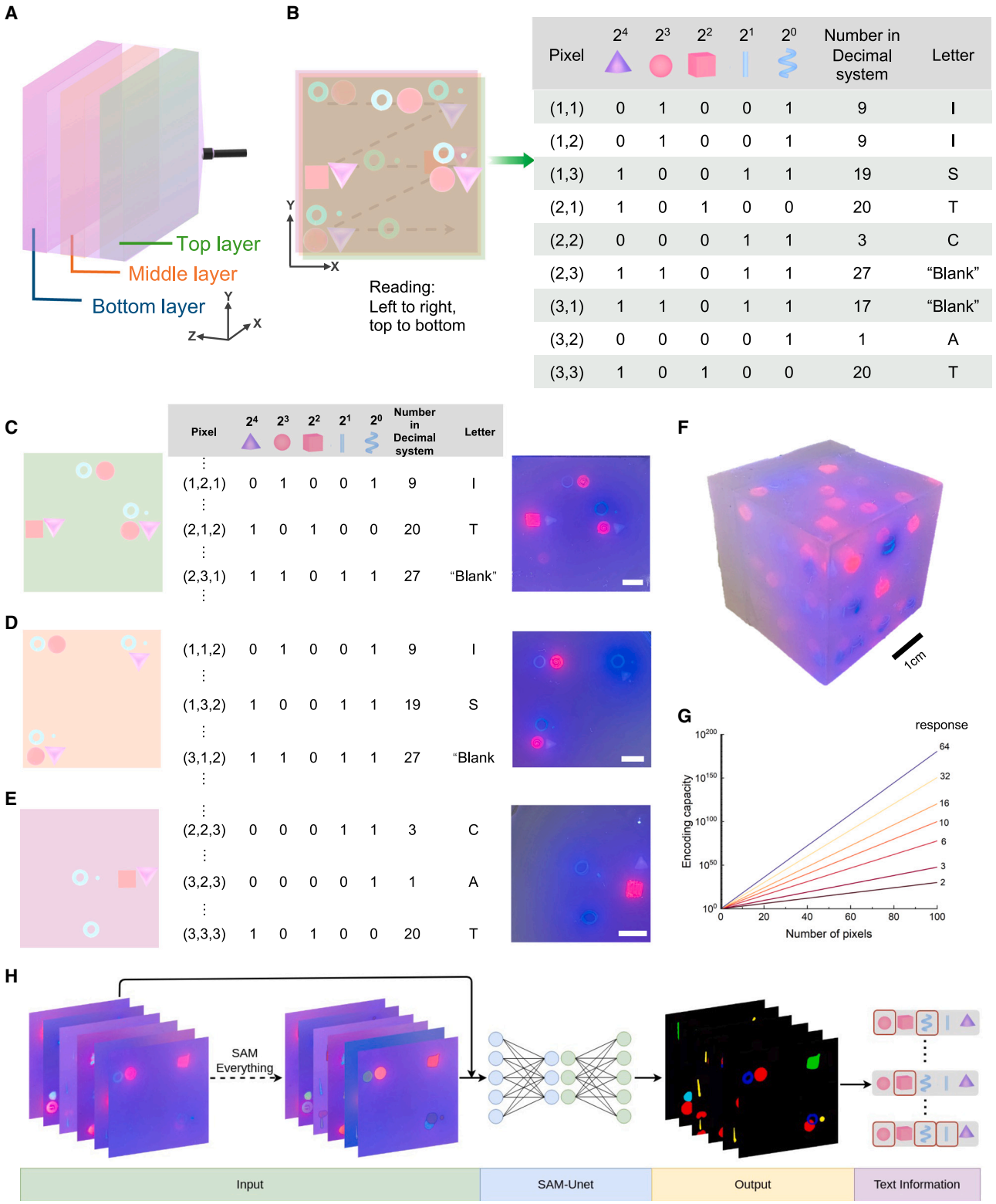

Pixel	2^4	2^3	2^2	2^1	2^0	Number in Decimal system	Letter
(1,1)	0	1	0	0	1	9	I
(1,2)	0	1	0	0	1	9	I
(1,3)	1	0	0	1	1	19	S
(2,1)	1	0	1	0	0	20	T
(2,2)	0	0	0	1	1	3	C
(2,3)	1	1	0	1	1	27	“Blank”
(3,1)	1	1	0	1	1	17	“Blank”
(3,2)	0	0	0	0	1	1	A
(3,3)	1	0	1	0	0	20	T

Pixel	2^4	2^3	2^2	2^1	2^0	Number in Decimal system	Letter
(1,2,1)	0	1	0	0	1	9	I
(2,1,2)	1	0	1	0	0	20	T
(2,3,1)	1	1	0	1	1	27	“Blank”
(1,1,2)	0	1	0	0	1	9	I
(1,3,2)	1	0	0	1	1	19	S
(3,1,2)	1	1	0	1	1	27	“Blank
(2,2,3)	0	0	0	1	1	3	C
(3,2,3)	0	0	0	0	1	1	A
(3,3,3)	1	0	1	0	0	20	T

Figure 4. Design and verification process of the physical unclonable function

(A) Schematic of the 3D matrix system.

(B) Fluorescent structures viewed from the 2D top plane (XY plane) and the associated decoding process.

(legend continued on next page)

between an input and a response through a stochastic and unclonable physical system. Its encoding and decoding capabilities depend solely on the number of "taggants" and "sampling points." The number of taggants determines the maximum number of ciphers, while the number of sampling points defines the maximum amount of readable content. In this work, we employ a binary-based coding language for decoding to encompass all original ciphers and facilitate future AI-based ciphers. The maximum cipher capacity is $2^n - 1$, where n is the number of taggants. For example, if using the English alphabet as the codebook, the encryption system requires only five taggants to cover all 26 letters. As illustrated in Figure S23, encoding the word "HYDROGEL" requires at least a 3 × 3 matrix to accommodate the sampling points and represent the full content, whereas encoding "HI" necessitates only a 2 × 2 matrix. Due to the ability to design a large number of taggants by combining various colors and geometries of printed structures, our fluorescent-responsive embedded printing method is adaptable to different codebooks with diverse cipher contents. For example, when the paragraph in Figure S24 is considered as a codebook, the encrypted information is "大家好,我是学生" (meaning "Hello everyone, I am a student" in Chinese), demonstrating that this technique is universally applicable to encryption in any language system.

Interestingly, in addition to realizing PUF encryption based on a 2D pattern, the embedded printing fluorescent encryption system can extend to hierarchical encryption based on 3D structures. We constructed a 3 × 3 × 3 3D sampling system (Figure 4A), using the codebook in Figure S25. When viewed from right to left, the overall pattern (Figure 4B) initially appears to contain the encrypted information "IISTC AT," which is incorrect. This incorrect information arises because decryption must consider the order in both the 2D plane and the 3D direction. The encrypted information printed in the top, center, and bottom layers is "IT," "IS," and "CAT," respectively (Figures 4C–4E), so the correct information is "IT IS CAT." The purpose of this hierarchical encryption is to enable on-demand decryption, significantly increasing the difficulty of deciphering the corresponding information. Unlike hierarchical encryption limited to the sampling points of the 2D plane (only 9), embedded printing constructs 3D encrypted messages across the entire 3D spatial sampling points (as many as 27). According to the deciphering principle of "left to right, top to bottom" and using the codebook in Figure S25, the encrypted message is "HI, IMPERIAL COLLEGE LONDON" (Figures 4F and S26). If this same content was encrypted using a 2D plane, at least a 6 × 6 matrix would be required to accommodate all sampling points and convey the information (including spaces between words). However, with 3D encryption technology, it only occupies a 3 × 3 × 3 matrix, effectively reducing the space required. Furthermore, the number of taggants can be infinitely expanded due to the diversity of colors and print structures of fluorescent ink, increasing both the encoding capacity and security level (Figure 4G). These experimental results demonstrate that the combination of embedded printing of fluorescent-responsive structures and PUF can efficiently encrypt information, making it an ideal technique for encryption and anti-counterfeiting applications.

Significant progress has been made in image segmentation using AI. Large models based on deep learning, such as SAM (Segment Anything Model) and Segmenter, have achieved impressive segmentation results on both natural and medical images.[47,48] These models are pre-trained on vast datasets of natural images, ensuring effective feature extraction and high segmentation accuracy. In this study, we further introduce AI to automatically identify fluorescent information by converting 3D fluorescent data into corresponding textual information (Figure 4H). The data used in the model include seven cubic samples, each exposed to UV light to collect surface fluorescence information from six surfaces. The fluorescent surface data were then randomly divided, with 80% used as the training set and 20% as the test set. Decoding surface fluorescence information into text information can be accomplished by either a classification or a segmentation task, for which different models are built in this paper for comparison.

For the classification task, the ResNet model was adopted, which is a classic framework in the classification field.[33] The input of the model is a fluorescent surface, and the classification label is whether the sample contains a certain type of fluorescent information. The accuracy of the ResNet model on the test set is 0.65. For the segmentation task, the segmentation label needs to be obtained at first. To obtain the segmentation label quickly, the "segment everything" module of SAM was employed to pre-segment the collected fluorescence data, effectively extracting the outlines of the fluorescent information. However, since the SAM pre-training dataset consists of natural images and does not include fluorescent images or definitions of fluorescent information, it struggled to accurately categorize similar types of fluorescent information, sometimes misidentifying different categories as the same object (Figure S28A). Consequently, manual modification of the pre-segmentation results was necessary to obtain accurate segmentation labels, which were then used to train the segmentation model. The segmentation model is based on SAM-UNet (Figure S29), a classic framework widely used in the field of image segmentation. To reduce training difficulty, the input to SAM-UNet included both the fluorescent surfaces and the corresponding pre-segmentation results from the SAM model. This integration allowed us to leverage the features extracted by the SAM model within the UNet network. The final SAM-UNet model achieved a segmentation dice score of 0.83 on the test set. To further assess the robustness of the SAM-UNet model, we subjected the sample to UV light at various positions. The images captured, presented in Figure S27, clearly show variations in fluorescence intensity at different distances. The SAM-UNet model achieved a Dice score of 0.817 on this test set, demonstrating its robustness.

(C–E) Schematics and photographs of the embedded fluorescent structures in layers at different depths: (C) top layer, scale bar: 0.5 cm; (D) center layer, scale bar: 0.5 cm; (E) bottom layer, scale bar: 0.5 cm.
(F) Isometric view of a 3D cube with internal fluorescent structures.
(G) Encoding capacity of the designed physical unclonable function.
(H) Illustration of the decoding process using AI.

Further analysis is required to decode the segmentation results into textual information. Fluorescent information from units located at the center of an edge is interfered with by information from adjacent surfaces (Figure S28B, red arrow), and units located at a corner are interfered with by information from adjacent edges (Figure S28B, green arrow). Therefore, the decoding sequence starts from the units at the centers of surfaces, followed by those at the centers of edges, and finally those at the corners. It is important to note that units at the centers of edges appear on two surfaces, while units at the corners appear on three surfaces. To improve decoding accuracy, information from different surfaces should be combined. For example, the unit in the red box located at the edge center (Figure S28C) shows a red square on the front surface but no red square segmentation information on the right surface, indicating that this unit does not contain a red square. Similarly, the unit in the green box at the corner shows a red ball on the front surface and a red square on the right surface but no red ball or red square information on the top surface, indicating that this unit does not contain a red ball or red square. The decryption method described above allows us to convert the fluorescence information into the textual one in a few seconds (Video S5 and Video S6). For the ResNet (classification result) and SAM-UNet (segmentation result), the accuracy rates for converting the fluorescence information of the samples into text are 0.61 and 0.81, respectively. Compared with the classification results, we can see that segmentation provides a large improvement in the text recognition accuracy rate. This can be attributed to the fact that the segmentation model requires pixel-level segmentation labels containing more semantic information during training. Although the acquisition of segmentation labels takes some time and effort, the process can be accelerated with the help of the SAM model. In addition, the classification results come from an end-to-end training process without post-processing, whereas in the segmentation task, post-processing can be used to improve the accuracy. As shown in Figure S30, there are small broken dots in the segmentation result that can be removed when their area is smaller than the specified minimum area in post-processing.

The above PUF design and authentication concept can be used for specific use cases.[25,36,49,50] For instance, our PUFs can work in secure packaging and ensure that the integrity of the packaging can be verified without physical tampering, which is crucial for industries such as pharmaceuticals and electronics. The integration of PUFs in advanced medical devices can help in the authentication of critical device components, ensuring that only genuine parts are used, thereby enhancing patient safety. Moreover, for highly secure documentation, our encryption method adds a layer of security that is virtually impossible to replicate without the exact decryption sequence, which involves considering both the 2D plane and the 3D volume, as demonstrated in Figure 4B. Here, superficially the information reads "IISTC AT," but the correct decryption "IT IS CAT" is only revealed when the encoded dimensions are fully considered. These possible applications illustrate the capabilities of our technology and its potential for enhancing security and functionality in real-world scenarios. Our approach demonstrated the feasibility of preparing centimeter-scale samples using a cost-effective 3D printer capable of producing parts that are up to tens of centimeters in size. This printer, while more expensive than conventional inkjet printers,[19,51] remains significantly less costly than photolithography setups,[24] striking a balance between affordability and functionality for larger-scale applications. The comparative analysis with other encryption and anti-counterfeiting technologies (Table S2) underscores the potential for scaling up this 3D encryption method for mass production while maintaining excellent thermal, physical, and chemical stability. One of the primary challenges in scaling up involves maintaining the clarity of the PDMS matrix to ensure that the fluorescent information is transmitted clearly, without distortion. The matrix, a mixture of two types of PDMS, is inherently translucent and requires a critical defoaming step during the manufacturing process. This step is crucial to prevent air bubbles, which can obscure the fluorescent patterns under UV light. We have also initiated pilot tests to further explore the scalability of this method, focusing on optimizing the mixing and curing processes to enhance the visibility and integrity of the encrypted data in larger batches. These efforts are aimed at overcoming the technical challenges associated with scaling up, ensuring that our method remains viable for industrial applications where clarity and precision are paramount.

Here, we introduce a versatile method capable of generating QR codes that can be swiftly decrypted using readily available portable devices like smartphones, and complex 3D encrypted messages in the form of specialized PUFs that enhance cipher capacity and decryption efficiency. To address the potential limitations associated with the use of specialized decryption equipment, we have integrated an AI-based model that allows for rapid and efficient decryption and enables a dynamic interaction between the material properties and AI technologies. By enabling material-AI interactions, our approach is tailored to fit scenarios where human operators are replaced by automated systems, ensuring that our encryption techniques remain relevant and effective in unmanned environments. While our system does utilize specialized materials, the overall advantages and potential applications significantly outweigh the initial perceived limitations, particularly when considering the enhanced security and versatility offered by our encryption techniques in an increasingly automated world.

Conclusion

In summary, our research introduces a novel multidimensional anti-counterfeiting technique that demonstrates the potential of combining structural manipulation at nano- to macro-levels with AI. The approach is based on the high-fidelity printing of 2D and 3D fluorescent hydrogel patterns within a PDMS matrix using direct ink writing. It takes advantage of the rheological adaptability of the matrix and ink to enable the stable and reliable embedding of encryption information in a flexible polymer, from 2D patterns such as watermarks or QR codes to complex 3D structures. Optimal post-curing ensures that the printed structures are securely implanted and that the matrix offers effective protection against the physicochemical agents that often degrade surface-based patterns. Even after applying mechanical stress, the encrypted information remains intact, and the fluorescent patterns swiftly revert to their original form. By

fine-tuning the type, concentration, and ratio of fluorescent materials in the ink down to the nano-level, we can control their visibility under different light wavelengths to create intricate, multicolored patterns. The integration of embedded 3D printing with hierarchical structures and the encoding principles of PUFs allows for the construction of multidimensional encrypted hydrogel composites. This approach not only enhances encoding capabilities but also enables precise, on-demand decryption leveraging PUFs. Compared to existing materials for anti-counterfeiting or information storage, our work underscores the significant potential of embedded printing assisted by AI recognition to achieve high precision and customizability. These results can open new paths to advance the integration of material-machine interaction functions.

METHODS

Materials

Pluronic F127, *p*-phenylenediamine, ethylenediamine, sodium citrate dihydrate, glycine, and hydrochloric acid were purchased from Sigma-Aldrich. Sodium chloride and sodium hydroxide were purchased from VWR. Two kinds of PDMS, Sylgard 184 and SE 1700, were purchased from Dow Corning. The commercial luminous powder and fluorescent paint were produced by DecorRom and Xiangyu, respectively.

Preparation of carbon quantum dots

The synthesis of quantum dots was based on a hydrothermal method in stainless-steel autoclaves. For the synthesis of R-CDs, 0.108 g *p*-phenylenediamine was dissolved in 15 mL ethanol. This solution was transferred in an autoclave with a 25-mL polytetrafluoroethylene (PTFE) liner, heated to 180°C for 16 h. The G-CDs were obtained by heating a solution of 0.108 g *p*-phenylenediamine, 0.15 g glycine, 30 μL ethylenediamine, and 15 mL water to 180°C for 8 h. For B-CDs, a solution containing 0.225 g sodium citrate dihydrate, 36 μL ethylenediamine, and 15 mL water was heated to 160°C for 8 h. To obtain pure CDs, these solutions were cooled down to room temperature after the reaction and passed through a PTFE filter (0.2 μm).

Preparation of the matrix and ink for embedded printing

The matrix for embedded printing is a mixture of two kinds of PDMS: Sylgard 184 and SE 1700. The mass ratio of the latter, which contains 20 wt % of fumed silica, in the matrix varies between 30 and 60 wt %. After being mixed homogeneously in a Thinky ARE-250 planetary mixer, the mixture was degassed in a desiccator under vacuum. The quantum dots were dispersed in the Pluronic F127 gel to obtain CD inks with Pluronic concentrations between 20 and 35 wt % and quantum dots concentration between 1 and 40 wt %. Similarly, inks containing luminous powder were prepared by adding 10 wt % of powder in 30 wt % Pluronic gel. For the ink with fluorescent paint, fumed silica (12–20 wt %) was added as a rheological modifier to obtain a printable ink. These inks were loaded in 3-mL syringe barrels and extruded through nozzles with diameters varying between 100 and 410 μm. Embedded printing was performed on a 3dInks direct ink writing system at room temperature.

Rheology test

A rheometer (TA Instruments Discovery HR-1) with 40-mm parallel stainless-steel geometry was used. The gap was 100 μm for the measurement of PDMS matrix and 1,000 μm for the ink. Flow tests were performed at a shear rate between 0.01 and 100 s^{-1}, and oscillatory tests were carried out at a frequency of 1 Hz.

Characterization

The UV-visible absorption spectra were conducted on a PerkinElmer UV/VIS spectrometer Lambda 25. The fluorescence intensity was tested using a PerkinElmer Fluorescence Spectrometer LS55. Optical images were captured with a Canon-EOS-760D. The geometry of the as-synthesized quantum dots was examined using transmission electron microscopy and atomic force microscopy. The fluorescence performance was observed under 365-nm UV lamps. Zwick Roell Z010 was used to conduct tensile and compression tests. The testing speed was 10 mm/min.

RESOURCE AVAILABILITY

Lead contact

Further information and requests for resources and reagents should be directed to and will be fulfilled by the lead contact, Ming Li (m.li19@alumni.imperial.ac.uk, mingli24@hku.hk).

Materials availability

This study did not generate new unique reagents.

Data and code availability

The main article and supplemental information contain all the data presented in the study. All modeling work was conducted in Python. All original code has been deposited at Github and is publicly available as of the date of publication at https://doi.org/10.5281/zenodo.14740339.

ACKNOWLEDGMENTS

This work was supported by the EPSRC Program Manufacture Using Advanced Powder Processes (MAPP) EP/P006566. S.Z. is supported by the China Scholarship Council (grant no. 201806120001). M.L. acknowledges financial assistance from Imperial College London in the form of the "President Scholarship" (grant no. 01790264). Q.G. appreciates the support from the China Scholarship Council (grant no. 202006440011).

AUTHOR CONTRIBUTIONS

S.Z. designed and executed the project. F.L. classified the data and trained the AI model. Q.G. and L.D. participated in synthesizing and characterizing the fluorescent quantum dots. M.L. conceived and guided the work and was involved in the writing of the manuscript. E.S. revised the content of the paper and provided useful suggestions. All authors discussed the contents and commented on the manuscript.

DECLARATION OF INTERESTS

The authors declare no competing interests.

SUPPLEMENTAL INFORMATION

Supplemental information can be found online at https://doi.org/10.1016/j.device.2025.100722.

Received: November 8, 2024
Revised: January 26, 2025
Accepted: February 4, 2025
Published: March 5, 2025

REFERENCES

1. Gu, L., Shi, H., Bian, L., Gu, M., Ling, K., Wang, X., Ma, H., Cai, S., Ning, W., Fu, L., et al. (2019). Colour-tunable ultra-long organic phosphorescence of a single-component molecular crystal. Nat. Photonics *13*, 406–411. https://doi.org/10.1038/s41566-019-0408-4.
2. Zhang, H., Hua, D., Huang, C., Samal, S.K., Xiong, R., Sauvage, F., Braeckmans, K., Remaut, K., and De Smedt, S.C. (2020). Materials and technologies to combat counterfeiting of pharmaceuticals: current and future problem tackling. Adv. Mater. *32*, 1905486. https://doi.org/10.1002/adma.201905486.
3. Phan-Quang, G.C., Han, X., Koh, C.S.L., Sim, H.Y.F., Lay, C.L., Leong, S.X., Lee, Y.H., Pazos-Perez, N., Alvarez-Puebla, R.A., and Ling, X.Y. (2019). Three-dimensional surface-enhanced Raman scattering platforms: large-scale plasmonic hotspots for new applications in sensing, microreaction, and data storage. Acc. Chem. Res. *52*, 1844–1854. https://doi.org/10.1021/acs.accounts.9b00163.
4. Huang, G., Xia, Q., Huang, W., Tian, J., He, Z., Li, B.S., and Tang, B.Z. (2019). Multiple Anti-Counterfeiting Guarantees from a Simple Tetraphenylethylene Derivative - High-Contrasted and Multi-State Mechanochromism and Photochromism. Angew. Chem. Int. Ed. Engl. *58*, 17814–17819. https://doi.org/10.1002/ange.201910530.
5. Arppe, R., and Sørensen, T.J. (2017). Physical unclonable functions generated through chemical methods for anti-counterfeiting. Nat. Rev. Chem *1*, 0031. https://doi.org/10.1038/s41570-017-0031.
6. Wei, C., Sun, Z., Huang, Y., and Li, L. (2018). Embedding anti-counterfeiting features in metallic components via multiple material additive manufacturing. Addit. Manuf. *24*, 1–12. https://doi.org/10.1016/j.addma.2018.09.003.
7. Lim, K.T.P., Liu, H., Liu, Y., and Yang, J.K.W. (2019). Holographic colour prints for enhanced optical security by combined phase and amplitude control. Nat. Commun. *10*, 25. https://doi.org/10.1038/s41467-018-07808-4.
8. Abdollahi, A., Roghani-Mamaqani, H., Razavi, B., and Salami-Kalajahi, M. (2020). Photoluminescent and chromic nanomaterials for anticounterfeiting technologies: recent advances and future challenges. ACS Nano *14*, 14417–14492. https://doi.org/10.1021/acsnano.0c07289.
9. Bian, F., Sun, L., Cai, L., Wang, Y., and Zhao, Y. (2020). Bioinspired MXene-integrated colloidal crystal arrays for multichannel bioinformation coding. Proc. Natl. Acad. Sci. USA *117*, 22736–22742. https://doi.org/10.1073/pnas.2011660117.
10. Li, M., Li, W., Cai, W., Zhang, X., Wang, Z., Street, J., Ong, W.-J., Xia, Z., and Xu, Q. (2019). A self-healing hydrogel with pressure sensitive photoluminescence for remote force measurement and healing assessment. Mater. Horiz. *6*, 703–710. https://doi.org/10.1039/c8mh01441h.
11. Li, J., Bisoyi, H.K., Lin, S., Guo, J., and Li, Q. (2019). 1, 2-Dithienyldicyanoethene-based, visible-light-driven, chiral fluorescent molecular switch: rewritable multimodal photonic devices. Angew. Chem. Int. Ed. Engl. *58*, 16052–16056. https://doi.org/10.1002/anie.201908832.
12. Ko, C.C., and Yam, V.W.W. (2018). Coordination Compounds with Photochromic Ligands: Ready Tunability and Visible Light-Sensitized Photochromism. Acc. Chem. Res. *51*, 149–159. https://doi.org/10.1021/acs.accounts.7b00426.
13. Li, Z., Chen, H., Li, B., Xie, Y., Gong, X., Liu, X., Li, H., and Zhao, Y. (2019). Photoresponsive luminescent polymeric hydrogels for reversible information encryption and decryption. Adv. Sci. *6*, 1901529. https://doi.org/10.1002/advs.201901529.
14. He, R., Yang, Y., Zhou, Q., Chang, S., Cheng, Y., Ma, X., Shi, Y., Zheng, L., and Cao, Q. (2024). Regulating room temperature phosphorescence of carbazole quaternization pyridine in polymer through Hofmeister effect. Aggregate *5*, e611. https://doi.org/10.1002/agt2.611.
15. Cai, W., Zhang, T., Xu, M., Zhang, M., Guo, Y., Zhang, L., Street, J., Ong, W.-J., and Xu, Q. (2019). Full color carbon dots through surface engineering for constructing white light-emitting diodes. J. Mater. Chem. C Mater. *7*, 2212–2218. https://doi.org/10.1039/c9tc00274j.
16. Chen, X., Zhang, J., Zhang, L., Tang, Q., Chen, Y., Guo, W., and Chang, L. (2024). In-situ controllable synthesis of carbon dots for patterned fluorescent wood films rapid fabrication strategy. Aggregate *5*, e519. https://doi.org/10.1002/agt2.519.
17. Qin, L., Liu, X., He, K., Yu, G., Yuan, H., Xu, M., Li, F., and Yu, Y. (2021). Geminate labels programmed by two-tone microdroplets combining structural and fluorescent color. Nat. Commun. *12*, 699. https://doi.org/10.1038/s41467-021-20908-y.
18. Zhao, Y., Zhao, X., Li, M.D., Li, Z., Peng, H., and Xie, X. (2020). Crosstalk-Free Patterning of Cooperative-Thermoresponse Images by the Synergy of the AIEgen with the Liquid Crystal. Angew. Chem. *132*, 10152–10158. https://doi.org/10.1002/ange.201915053.
19. Wang, Q., Lin, B., Chen, M., Zhao, C., Tian, H., and Qu, D.H. (2022). A dynamic assembly-induced emissive system for advanced information encryption with time-dependent security. Nat. Commun. *13*, 4185. https://doi.org/10.1038/s41467-022-31978-x.
20. Andres, J., Hersch, R.D., Moser, J.E., and Chauvin, A.S. (2014). A New Anti-Counterfeiting Feature Relying on Invisible Luminescent Full Color Images Printed with Lanthanide-Based Inks. Adv. Funct. Mater. *24*, 5029–5036. https://doi.org/10.1002/adfm.201400298.
21. Su, G., Li, Z., Gong, J., Zhang, R., Dai, R., Deng, Y., and Tang, B.Z. (2022). Information-Storage Expansion Enabled by a Resilient Aggregation-Induced-Emission-Active Nanocomposite Hydrogel. Adv. Mater. *34*, 2207212. https://doi.org/10.1002/adma.202207212.
22. Le, X., Shang, H., Wu, S., Zhang, J., Liu, M., Zheng, Y., and Chen, T. (2021). Heterogeneous Fluorescent Organohydrogel Enables Dynamic Anti-Counterfeiting. Adv. Funct. Mater. *31*, 2108365. https://doi.org/10.1002/adfm.202108365.
23. Fischer, J., and Wegener, M. (2012). Three-dimensional optical laser lithography beyond the diffraction limit. Laser Photon. Rev. *7*, 22–44. https://doi.org/10.1002/lpor.201100046.
24. Ritacco, T., Lio, G.E., Xu, X., Broussier, A., Issa, A., Giocondo, M., Bachelot, R., Blaize, S., Couteau, C., and Jradi, S. (2021). Three-Dimensional Photoluminescent Crypto-Images Doped with (CdSe)ZnS Quantum Dots by One-Photon and Two-Photon Polymerization. ACS Appl. Nano Mater. *4*, 6916–6927. https://doi.org/10.1021/acsanm.1c00968.
25. Li, J., Liu, R., Lin, H., Ye, S., Ye, M., Wang, X., and Zhu, X. (2021). Tensor Network-Encrypted Physical Anti-counterfeiting Passport for Digital Twin Authentication. ACS Appl. Mater. Interfaces *13*, 61536–61543. https://doi.org/10.1021/acsami.1c18808.
26. Mayer, F., Richter, S., Hübner, P., Jabbour, T., and Wegener, M. (2017). 3D Fluorescence-Based Security Features by 3D Laser Lithography. Advanced Materials Technologies *2*, 1700212. https://doi.org/10.1002/admt.201700212.
27. Mayer, F., Richter, S., Westhauser, J., Blasco, E., Barner-Kowollik, C., and Wegener, M. (2019). Multimaterial 3D laser microprinting using an integrated microfluidic system. Sci. Adv. *5*, eaau9160. https://doi.org/10.1126/sciadv.aau9160.
28. Grosskopf, A.K., Truby, R.L., Kim, H., Perazzo, A., Lewis, J.A., and Stone, H.A. (2018). Viscoplastic Matrix Materials for Embedded 3D Printing. ACS Appl. Mater. Interfaces *10*, 23353–23361. https://doi.org/10.1021/acsami.7b19818.
29. Mahmoudi, M., Burlison, S.R., Moreno, S., and Minary-Jolandan, M. (2021). Additive-Free and Support-Free 3D Printing of Thermosetting Polymers with Isotropic Mechanical Properties. ACS Appl. Mater. Interfaces *13*, 5529–5538. https://doi.org/10.1021/acsami.0c19608.

30. Truby, R.L., Wehner, M., Grosskopf, A.K., Vogt, D.M., Uzel, S.G.M., Wood, R.J., and Lewis, J.A. (2018). Soft Somatosensitive Actuators via Embedded 3D Printing. Adv. Mater. *30*, e1706383. https://doi.org/10.1002/adma.201706383.

31. Nelson, A.Z., Kundukad, B., Wong, W.K., Khan, S.A., and Doyle, P.S. (2020). Embedded droplet printing in yield-stress fluids. Proc. Natl. Acad. Sci. USA *117*, 5671–5679. https://doi.org/10.1073/pnas.1919363117.

32. Qian, M., Du, Y., Wang, S., Li, C., Jiang, H., Shi, W., Chen, J., Wang, Y., Wagner, E., and Huang, R. (2018). Highly Crystalline Multicolor Carbon Nanodots for Dual-Modal Imaging-Guided Photothermal Therapy of Glioma. ACS Appl. Mater. Interfaces *10*, 4031–4040. https://doi.org/10.1021/acsami.7b19716.

33. He, K., Zhang, X., Ren, S., and Sun, J. (2016). Deep residual learning for image recognition. In Proceedings of the IEEE conference on computer vision and pattern recognition (IEEE), pp. 770–778. https://doi.org/10.1109/CVPR.2016.90.

34. He, K., Zhang, X., Ren, S., and Sun, J. (2015). Delving deep into rectifiers: Surpassing human-level performance on imagenet classification. In Proceedings of the IEEE international conference on computer vision (IEEE), pp. 1026–1034. https://doi.org/10.1109/ICCV.2015.123.

35. Ren, S., He, K., Girshick, R., and Sun, J. (2017). Faster r-cnn: Towards real-time object detection with region proposal networks. IEEE Trans. Pattern Anal. Mach. Intell. *39*, 1137–1149. https://doi.org/10.1109/TPAMI.2016.2577031.

36. Zhang, J., Liu, Y., Njel, C., Ronneberger, S., Tarakina, N.V., and Loeffler, F.F. (2023). An all-in-one nanoprinting approach for the synthesis of a nanofilm library for unclonable anti-counterfeiting applications. Nat. Nanotechnol. *18*, 1027–1035. https://doi.org/10.1038/s41565-023-01405-3.

37. Feilden, E., Blanca, E.G.-T., Giuliani, F., Saiz, E., and Vandeperre, L. (2016). Robocasting of structural ceramic parts with hydrogel inks. J. Eur. Ceram. Soc. *36*, 2525–2533. https://doi.org/10.1016/j.jeurceramsoc.2016.03.001.

38. Lee, J., Chae, S., Lee, H., and Kim, G.H. (2020). A 3D printing strategy for fabricating in situ topographical scaffolds using pluronic F-127. Addit. Manuf. *32*, 101023. https://doi.org/10.1016/j.addma.2019.101023.

39. Zhou, S., Tirichenko, I.S., Zhang, X., Hong, Y., Payne, H., Withers, P.J., Bouville, F., and Saiz, E. (2024). Embedded 3D printing of microstructured multi-material composites. Matter *7*, 668–684. https://doi.org/10.1016/j.matt.2023.10.031.

40. Friedrich, L.M., and Seppala, J.E. (2021). Simulated filament shapes in embedded 3D printing. Soft Matter *17*, 8027–8046. https://doi.org/10.1039/d1sm00731a.

41. Friedrich, L.M., Gunther, R.T., and Seppala, J.E. (2022). Suppression of Filament Defects in Embedded 3D Printing. ACS Appl. Mater. Interfaces *14*, 32561–32578. https://doi.org/10.1021/acsami.2c08047.

42. Grosskopf, A.K., Truby, R.L., Kim, H., Perazzo, A., Lewis, J.A., and Stone, H.A. (2018). Viscoplastic matrix materials for embedded 3D printing. ACS Appl. Mater. Interfaces *10*, 23353–23361. https://doi.org/10.1021/acsami.7b19818.

43. Herschel, W.H., and Bulkley, R. (1926). Konsistenzmessungen von Gummi-Benzollösungen. Kolloid Z. *39*, 291–300. https://doi.org/10.1007/BF01432034.

44. Vadnere, M., Amidon, G., Lindenbaum, S., and Haslam, J. (1984). Thermodynamic studies on the gel-sol transition of some pluronic polyols. Int. J. Pharm. *22*, 207–218. https://doi.org/10.1016/0378-5173(84)90022-X.

45. Rassing, J., and Attwood, D. (1982). Ultrasonic velocity and light-scattering studies on the polyoxyethylene polyoxypropylene copolymer Pluronic F127 in aqueous solution. Int. J. Pharm. *13*, 47–55. https://doi.org/10.1016/0378-5173(82)90141-7.

46. Weeks, R.D., Truby, R.L., Uzel, S.G.M., and Lewis, J.A. (2023). Embedded 3D Printing of Multimaterial Polymer Lattices via Graph-Based Print Path Planning. Adv. Mater. *35*, e2206958. https://doi.org/10.1002/adma.202206958.

47. Kirillov, A., Mintun, E., Ravi, N., Mao, H., Rolland, C., Gustafson, L., Xiao, T., Whitehead, S., Berg, A.C., and Lo, W.-Y. (2023). Segment anything. In Proceedings of the IEEE/CVF International Conference on Computer Vision (IEEE), pp. 4015–4026. https://doi.org/10.1109/ICCV51070.2023.00371.

48. Strudel, R., Garcia, R., Laptev, I., and Schmid, C. (2021). Segmenter: Transformer for Semantic Segmentation. In Proceedings of the IEEE/CVF international conference on computer vision (IEEE), pp. 7262–7272. https://doi.org/10.1109/ICCV48922.2021.00717.

49. Gu, Y., He, C., Zhang, Y., Lin, L., Thackray, B.D., and Ye, J. (2020). Gap-enhanced Raman tags for physically unclonable anticounterfeiting labels. Nat. Commun. *11*, 516. https://doi.org/10.1038/s41467-019-14070-9.

50. Fei, J., and Liu, R. (2016). Drug-laden 3D biodegradable label using QR code for anti-counterfeiting of drugs. Mater. Sci. Eng., C *63*, 657–662. https://doi.org/10.1016/j.msec.2016.03.004.

51. Huang, W., Xu, M., Liu, J., Wang, J., Zhu, Y., Liu, J., Rong, H., and Zhang, J. (2019). Hydrophilic Doped Quantum Dots "Ink" and Their Inkjet-Printed Patterns for Dual Mode Anticounterfeiting by Reversible Cation Exchange Mechanism. Adv. Funct. Mater. *29*, 1808762. https://doi.org/10.1002/adfm.201808762.